

Chapter 2

Field-Effect Self-Mixing Mechanism and Detector Model

Abstract Self-mixing of terahertz electromagnetic wave occurs in a field-effect electron channel when the terahertz electric field modulates both the local electron density and the drift velocity. In order to realize sensitive terahertz detection, asymmetry in the electric field and/or the charge density is required for generation of a unidirectional photocurrent/voltage. Existing hydrodynamic detection theories are reviewed and discussed. A detector model taking into account the spatial distributions of both the terahertz electric field and the electron density in the gated electron channel is developed in this chapter. The model presents full detector characteristics when both a source–drain bias and a gate voltage are applied. The model suggests that an asymmetric distribution of terahertz electric field is preferred for high-responsivity terahertz detection without a source–drain bias. The strength of terahertz photore-sponse is characterized by the self-mixing factor and the field-effect factor. The former factor can be optimized by a strongly asymmetric and enhanced terahertz near field by using asymmetric terahertz antennas. Simulations based on the FDTD method confirm the effectiveness of asymmetric antenna design and the low-pass filter to isolate the antenna blocks from the electrical bonding pads for the detector.

2.1 The Physics of Terahertz Plasmon Detection

Plasmon in low-dimensional semiconductor structures has long been considered as an active medium for the detection and emission of terahertz electromagnetic waves. Plasmons as collective charge-density waves can be manipulated by tuning the electron density and by constructing specific plasma-wave cavities. In gated electron channels based on high-electron-mobility, two-dimensional electron gas (2DEG) tunable plasmon cavities can be formed. The interactions among the plasma wave, the terahertz electromagnetic wave, and the electron transport may be implemented in devices for high-sensitivity terahertz detection and high-efficiency terahertz emission. In this section, a review of the existing theories on plasmons in field-effect electron channel for detection is presented.

M.I. Dyakonov and M.S. Shur proposed terahertz emission in 1993 [1] and detection in 1996 [2] in gated 2DEG devices. The field-effect channel with a gate length

of L defines the plasmon cavity. Assuming the plasmon cavity has a ‘short-circuit’ boundary on the left side and an ‘open-circuit’ boundary on the right side, the frequencies of the eigen plasmon modes are given as

$$\omega_N = (2N - 1)\omega_0, \quad (2.1)$$

$$\omega_0 = \frac{\pi}{2L} \sqrt{\frac{e(U_g - U_{th})}{m^*}}, \quad (2.2)$$

where $N = 1, 2, \dots$. Each eigen mode corresponds to an odd number of quarter wave length, i.e.,

$$L = (2N - 1) \frac{\lambda_p}{4}, \quad (2.3)$$

$$\lambda_p = \frac{2\pi s}{\omega_p}, \quad (2.4)$$

$$s = \sqrt{\frac{e(U_g - U_{th})}{m^*}}, \quad (2.5)$$

where λ_p is the plasma wave length, s is the plasma wave velocity, U_g is the gate voltage, U_{th} is the threshold voltage to pinch-off the 2DEG, e and m^* are the electron charge and effective mass, respectively. The plasmon modes can be tuned by the size of the cavity, i.e., the gate length L , and the electron density through the gate voltage. In a submicrometer-sized plasmon cavity, the plasmon frequency can be tuned into terahertz frequency range [2].

The asymmetric boundary condition and hence the quarter-wavelength nature of the plasmon cavity are preferred for both terahertz emission and detection. For emitters, self-excitation of plasma oscillations may be induced by electrons moving through the plasmon cavity under an external DC electric field [1]. For detectors, the asymmetry boundary conditions are essential to the generation of a unidirectional photocurrent or photovoltage. An intuitive picture of plasmon detection can be illustrated as follows. A terahertz electromagnetic wave with frequency ω excites resonantly/nonresonantly plasma waves in the channel. Electrons in the channel driven by the longitudinal electric field accompanied with the plasma wave under asymmetric boundary conditions induce a unidirectional current through the channel or equivalently a DC voltage across the source and the drain electrodes [2].

The excitation of plasmon modes in the gated electron channel depends on the quality factor of the specific mode

$$Q_p = \omega_p \tau_p, \quad (2.6)$$

where, τ_p is the lifetime of the plasmon mode. The higher the quality factor, the easier the plasmon can be excited by either the incident terahertz wave or drifting electrons through the cavity. Resonant excitation of plasmon can be achieved when $Q_p = \omega_p \tau_p \gg 1$. In contrast, plasmon modes are overdamped when $Q_p = \omega_p \tau_p \ll 1$.

For the existing semiconductors, the quality factor is usually at the intermediate level, i.e., $\omega_p \tau_p \approx 1\text{--}10$. The nonresonant terahertz detection was observed in a GaAs HEMT device for the first time in 1998 [3]. Later on, nonresonant detection was achieved in short channel HEMT devices and CMOS devices [4–8]. As shown in Fig. 2.1, a typical nonresonant response is tuned by the gate voltage at 300 K [7]. Meanwhile, resonant terahertz detection was demonstrated in GaAs HEMTs and double-quantum-well (DQW) FETs [9–14]. A typical resonant response at 10 K as a function of the gate voltage is shown in Fig. 2.2 [10].

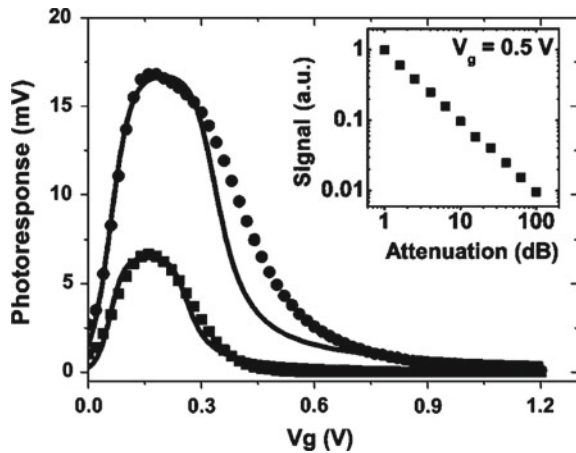
The physics behind the observed terahertz photoresponse can be illustrated in a model device where the terahertz field signal is applied between the gate and the source, as shown in Fig. 2.3. The nonlinear electron transport in the field-effect channel altered by the terahertz electric field gives rise to a photovoltage/current across/through the channel. M.I. Dyakonov and M.S. Shur studied the detection of terahertz electromagnetic wave in a field-effect transistor without an externally applied source–drain bias, i.e., in the linear regime of the field-effect transistor [2]. Veksler et al. extended the theory to the case when the electrons are driven by a DC current (a finite source–drain bias is applied between the drain and the source) [15]. It is found that the terahertz response can be strongly enhanced by the driving current, especially when the current reaches the saturation current. Here, we review the main results of these theoretical works as a starting point for our modeling on the terahertz detection in field-effect electron channel.

The governing equations for electrons in the channel are the hydrodynamic Euler equation of inertial motion and the continuity equation of electron flow

$$\frac{\partial v}{\partial t} + v \frac{\partial v}{\partial x} + \frac{v}{\tau} + \frac{e}{m^*} \frac{\partial U}{\partial x} = 0, \quad (2.7)$$

$$\frac{\partial n}{\partial t} + \frac{\partial (nv)}{\partial x} = 0, \quad (2.8)$$

Fig. 2.1 Nonresonant terahertz response as a function of the gate voltage for two transistors with 600 nm (*squares*) and 800 nm (*circles*) gates at 120 GHz. *Inset* shows the signal versus attenuation for the gate voltage 0.5 V. Reprinted with permission of Ref. [7], copyright 2004, American Institute of Physics



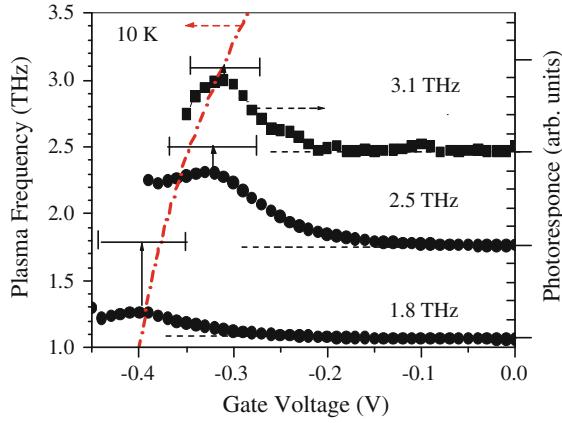


Fig. 2.2 Resonant terahertz response of an InGaAs device as a function of the gate voltage at three different terahertz frequencies (1.8, 2.5 and 3.1 THz) at 10 K (*right axis*). Curves are shifted vertically for clarity. *Dashed lines* indicate the zero of the photoresponse. *Arrows* indicate resonance positions. Calculated plasmon frequency as a function of the gate voltage for $U_{th} = -0.41$ V is shown as the *dash-dotted line* (*left axis*). The *error bars* correspond to the linewidth of the observed resonance peaks. Reprinted with permission of Ref. [10], copyright 2006, American Institute of Physics

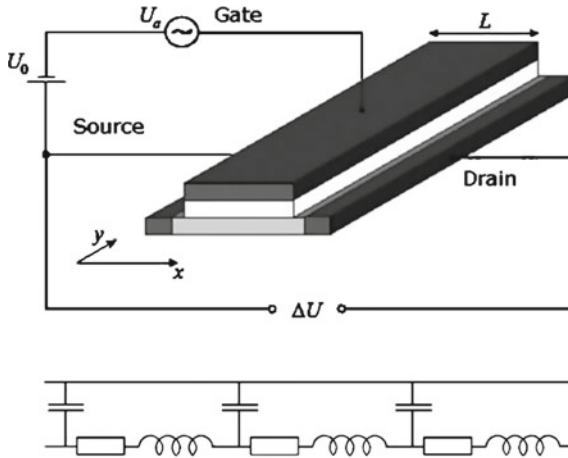


Fig. 2.3 A schematic and an equivalent circuit for the detector. Reprinted from Ref. [6], with kind permission of Springer Science + Business Media

where U is the local electrical potential in the channel, $-\partial U/\partial x$ is the local longitudinal electric field in the channel, v is the local electron velocity in direction of x , n is the local electron density, τ is the momentum relaxation time, e is the absolute value of the electron charge and m^* is the effective electron mass. In gradual channel

approximation (GCA), the local electron density n in the channel is related to the local channel potential U

$$n = \frac{C_g(U_g - U_{th} - U)}{e}, \quad (2.9)$$

where, C_g is the gate to channel capacitance per unit area, U_g is the gate–source voltage and U_{th} is the threshold gate voltage to pinch off the electron channel. Equation 2.8 can be written as

$$\frac{\partial U}{\partial t} + \frac{\partial(Uv)}{\partial x} = 0. \quad (2.10)$$

When a terahertz signal with a frequency of ω is applied between the source and the gate, plasma wave can be excited at the source side and travels toward the drain side with a speed of $s = \sqrt{e(U_g - U_{th})/m^*}$. The boundary conditions for Eqs. (2.7) and (2.10) can be different depending on whether a finite source–drain bias is applied or not. In the case when no source–drain bias is applied and the drain is connected to ground, the boundary conditions can be rewritten as

$$U(0) = U_g - U_{th} + U_a \cos \omega t, \quad (2.11)$$

$$v(L) = 0. \quad (2.12)$$

where U_a is the potential induced by the incident terahertz wave. In the case when a source–drain bias is applied and a source–drain current I_d flows through the electron channel, the boundary conditions can be written as [1, 2]

$$U(0) = U_g - U_{th} + U_a \cos \omega t, \quad (2.13)$$

$$v(L) = I_d / U(L) C_g W, \quad (2.14)$$

where W is the channel width. The above boundary conditions mean that the terahertz signal is fed into the detector only from the source side. This asymmetric condition can be realized by using various methods, e.g., asymmetric source and drain contacts, different source–gate and drain–gate distances, and asymmetric terahertz antennas as will be introduced in Sect. 2.3.2.

Equations (2.7) and (2.10) with the corresponding boundary conditions can be solved either analytically or numerically and the induced photovoltage between the source and drain can be obtained. It is not necessary to repeat the results for all situations. Here, we introduce the results for the case when no external source–drain bias is applied. For resonant situation in which $\omega\tau \gg 1$ and $s\tau/L \gg 1$, i.e., the damping of the excited plasma wave is small and the gated channel forms a cavity to support discrete plasma wave modes according to Eq. (2.1), the photovoltage as a function of the terahertz frequency has a Lorentzian line shape

$$\delta U \propto \left(\frac{s\tau}{L}\right)^2 \frac{1}{1 + 4(\omega - \omega_N)^2 \tau^2}. \quad (2.15)$$

In contrast, when $\omega\tau \ll 1$, i.e., the plasma wave is overdamped and the resonance is suppressed, the induced photovoltage is rather a smooth function of the frequency and the channel length

$$\delta U = \frac{1}{4} \frac{U_a^2}{U_g - U_{th}} \frac{\sinh^2 \kappa - \sin^2 \kappa}{\sinh^2 \kappa + \cos^2 \kappa}, \quad (2.16)$$

where, $\kappa = (L/s)(\omega/2\tau)^2$. In the special case when the channel length is much larger than the decay length of the plasma wave

$$L \gg s\left(\frac{\tau}{\omega}\right)^2, \quad (2.17)$$

the induced photovoltage has the form

$$\delta U = \frac{1}{4} \frac{U_a^2}{U_g - U_{th}} \left\{ 1 + \frac{2\omega\tau}{\sqrt{1 + \omega^2\tau^2}} \right\}, \quad (2.18)$$

i.e., independent on the channel length.

The photovoltage strongly depends on the nonlinearity in the field-effect controlled electron density. In the case when a source–drain bias is applied and a DC current $I_d \neq 0$ flows through the channel, the electron density varies from the source side to the drain side. Such a nonuniform spatial distribution of the electron density enhances the photoresponse. According to the theoretical analysis done by Veksler et al., the photovoltage tends to be infinitely high when the source–drain current reaches the saturation current [15]. For example, the $I - V$ characteristic and the nonresonant response at 200 GHz of a GaAs HEMT are shown in Fig. 2.4a and b,

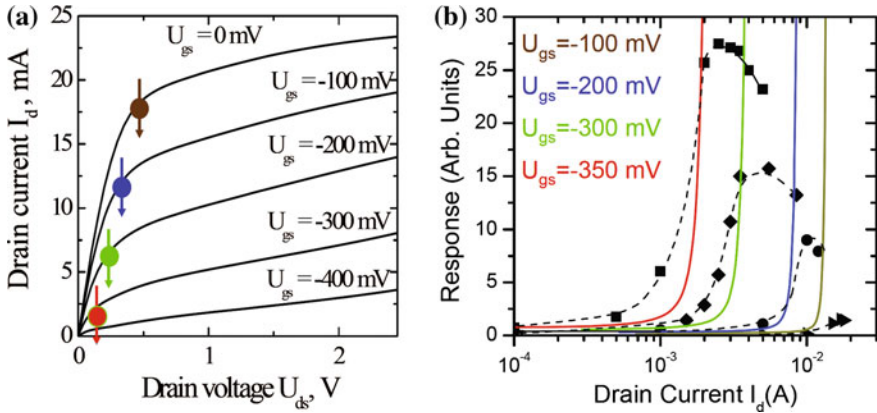


Fig. 2.4 **a** $I - V$ characteristics of a GaAs HEMT at different gate voltages. The *dots* correspond to the saturation voltage. **b** Terahertz response at 200 GHz as a function of the drain current. *Solid curves* represent the theoretical photovoltage. Reprinted with permission of Ref. [15], copyright 2006, American Physical Society

respectively. The photovoltage increases significantly, then reaches a maximum and finally decreases with increasing the drain current. Such a behavior is not recovered by the calculated photoresponse plotted as the solid curves in Fig. 2.4b.

The above theories provide clear pictures for different terahertz detection processes in the linear and saturation regimes of a field-effect transistor. However, they are inefficient in providing quantitative analyses of the photovoltage. The assumption that the terahertz signal is applied between the gate and the source and/or between the drain and the source neglects the detailed spatial distribution of the terahertz field. Possible interplay between the terahertz field and the electron channel with a nonuniform density is neglected as well. Therefore, it is of great importance to develop a detector model that takes into account both the spatial distributions of the terahertz field and the electron density. Such a detector model would provide full description of the photoresponses in the linear regime (LR), the saturation regime (SR), and the transition regime (TR). Above all, the model would provide guidance for the design and optimization of field-effect terahertz detectors.

2.2 Quasi-Static Self-Mixing Detector Model

As discussed in the previous section, the theories of terahertz detection based on field-effect transistors (FETs) assume an asymmetric terahertz field distribution across the gated electron channel in the first place. A clear physical picture of self-mixing mechanism is given by the resonant and nonresonant theories. However, no design rule for detector optimization is given. Furthermore, the theories do not clearly provide detector characteristics when both a gate voltage and a source–drain bias are applied [15]. Here, we present a detector model taking into account both the spatial distributions of the terahertz field and the charge density in the gated channel. The model is of quasi-static and is based on the gradual channel approximation (GCA). This model provides a full description of the detector response in the linear regime (LR), the saturation regime (SR), and the transition regime (TR). Optimized detector design can be made based on this model [16–22].

A schematic of the model detector and the equivalent circuit are given in Fig. 2.5. The active region of the detector is composed of a field-effect electron channel and terahertz antennas. According to GCA, the field-effect electron channel can be divided into a series of infinitely small segments of the electron channel. Under a source–drain bias V_{ds} , the current through the channel can be expressed as [23]

$$i_x = -eWn_x\mu \frac{dV_x}{dx} = -eWn_x(V_{\text{geff}})\mu \frac{dV_x}{dx}, \quad (2.19)$$

where μ is the electron mobility, W is the channel (2DEG mesa) width. We define $V_{\text{geff}} = V_g - V_{\text{th}} - V_x$ as the effective gate voltage at location x , where V_g and V_{th} are the applied DC gate voltage and the threshold gate voltage to pinch off the 2DEG. The channel potential V_x varies from 0 to V_{ds} from $x = 0$ to $x = L$. The local electron

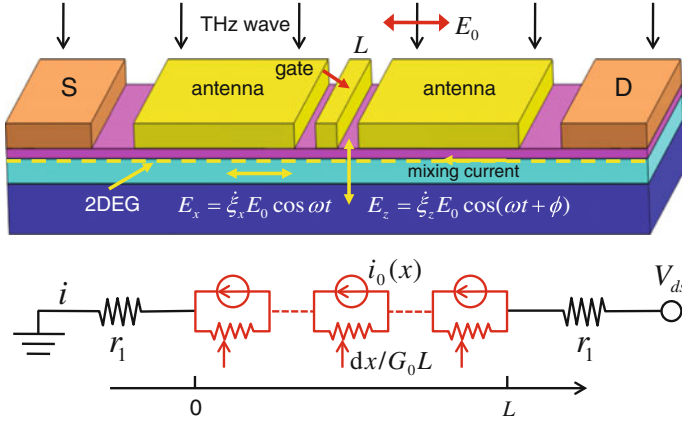


Fig. 2.5 A schematic and an equivalent circuit of the self-mixing detector. Reprinted with permission of Ref. [17], copyright 2012, American Institute of Physics

density is controlled by the effective local gate voltage: $n_x = C_g V_{\text{geff}}/e$, where C_g is the effective gate-channel capacitance per unit area. The total current through the electron channel can be expressed as

$$I_{\text{ds}} = \frac{1}{L} \int_0^L i_x dx = -\frac{eW\mu C_g}{L} \int_0^{V_{\text{ds}}} V_{\text{geff}} dV_x. \quad (2.20)$$

The drain–source current and the local channel potential can be further written as

$$I_{\text{ds}} = \begin{cases} \mu C_g W [2(V_g - V_{\text{th}})V_{\text{ds}} - V_{\text{ds}}^2]/2L & \text{if } V_{\text{ds}} \leq V_g - V_{\text{th}}, \\ \mu C_g W [(V_g - V_{\text{th}})^2 + \lambda(V_{\text{ds}} - V_g + V_{\text{th}})]/2L & \text{if } V_{\text{ds}} > V_g - V_{\text{th}}, \end{cases} \quad (2.21)$$

$$V_x = \begin{cases} (V_g - V_{\text{th}}) [1 - (1 - x/L_{\text{LR}})^{1/2}], x = [0, L] & \text{if } V_{\text{ds}} \leq V_g - V_{\text{th}}, \\ (V_g - V_{\text{th}}) [1 - (1 - x/L_{\text{SR}})^{1/2}], x = [0, L_{\text{SR}}] & \text{if } V_{\text{ds}} > V_g - V_{\text{th}}, \end{cases} \quad (2.22)$$

where, parameter λ describes the degree of the effective channel-length modulation $L \rightarrow L_{\text{SR}} = L/[1 + \lambda(V_{\text{ds}} - V_g + V_{\text{th}})/(V_g - V_{\text{th}})^2]$ in regime SR, and $L_{\text{LR}} = L(V_g - V_{\text{th}})^2/[2(V_g - V_{\text{th}})V_{\text{ds}} - V_{\text{ds}}^2]$ in regime LR.

From Eqs. (2.19), (2.21) and (2.22), the charge density and its derivative dn_x/dV_{geff} defined as field-effect factor at any location can be numerically calculated. In the case when $V_{\text{ds}} = 0$ V, the differential conductance can be simply written as

$$G_0 = e\mu \frac{W}{L} n(V_g - V_{\text{th}}). \quad (2.23)$$

For a realistic field-effect detector, there exists resistances from the ohmic contacts and the 2DEG mesa in series with the gated electron channel. These series resistances are absorbed into $2r_1$, as shown in Fig. 2.5.

Upon terahertz irradiation with a frequency of $\omega = 2\pi f$ and an energy flux of P_0 , both a horizontal ($\dot{\xi}_x E_0$) and a perpendicular ($\dot{\xi}_z E_0$) terahertz field in the channel are induced. Under the quasi-static assumption, i.e., $\omega\tau \ll 1$, the local effective channel potential and the effective gate voltage are modulated by the terahertz field and can be written as

$$V_x \rightarrow V_x + \xi_x E_0 \cos(\omega t), \quad (2.24)$$

$$V_g \rightarrow V_g + \xi_z E_0 \cos(\omega t + \phi), \quad (2.25)$$

where $\dot{\xi}_x = d\xi_x/dx$, $\dot{\xi}_z = d\xi_z/dz$ and ϕ are the horizontal and perpendicular field enhancement factors, and the phase difference between the induced fields, respectively. E_0 is determined by the incident energy flux and the free-space impedance Z_0 by $P_0 = E_0^2/2Z_0$.

Substituting Eqs. (2.24) and (2.25) into Eq. (2.19), we can get the current through the electron channel

$$i_x = e\mu W n (V_{\text{geff}} + \xi_z E_0 \cos(\omega t + \phi) - \xi_x E_0 \cos \omega t) \frac{d}{dx} (V_x + \xi_x E_0 \cos \omega t). \quad (2.26)$$

We assume that the total current can be obtained as

$$i_{\text{ds}} = \frac{1}{LT} \int_0^T dt \int_0^L dx i_x. \quad (2.27)$$

Where $T = 2\pi/\omega$ is the terahertz oscillating period. This assumption is valid for the case when the channel length is larger than the decay length of the plasma wave or in general the plasma wave excitation is confined in a small fraction of the gated channel. Furthermore, it is safely assumed that the incident terahertz power is low and the induced terahertz potential is small comparing to the applied gate voltage and the source-drain bias. The electron density can be expressed as

$$n = n(V_{\text{geff}}) + \frac{dn}{dV_{\text{geff}}} \xi_z E_0 \cos(\omega t + \phi) - \frac{dn}{dV_{\text{geff}}} \xi_x E_0 \cos \omega t. \quad (2.28)$$

By integrating i_x along the whole gated electron channel, we have

$$\begin{aligned} & \frac{1}{L} \int_0^L i_x dx \\ &= \frac{e\mu W}{L} \int_0^L \left[n(V_{\text{geff}}) + \frac{dn}{dV_{\text{geff}}} \xi_z E_0 \cos(\omega t + \phi) - \frac{dn}{dV_{\text{geff}}} \xi_x E_0 \cos \omega t \right] \\ & \quad \times \left[dV_x + \dot{\xi}_x E_0 \cos \omega t dx \right]. \end{aligned} \quad (2.29)$$

The time-averaged source-drain current can be obtained by averaging Eq. (2.29) in the oscillation period

$$i_{ds} = I_{ds} + i_{xz} + i_{xx}, \quad (2.30)$$

where, the first term is the DC bias current the same as that in Eq. (2.21), the rest are two different types of self-mixing current. The self-mixing photocurrent can be expressed as

$$i_{xz} = \frac{e\mu W}{2L} Z_0 P_0 \bar{z} \int_0^L \frac{dn}{dV_{\text{geff}}} \dot{\xi}_x \dot{\xi}_z \cos \phi \, dx, \quad (2.31)$$

$$i_{xx} = -\frac{e\mu W}{2L} Z_0 P_0 \int_0^L \frac{dn}{dV_{\text{geff}}} \xi_x \dot{\xi}_x \, dx, \quad (2.32)$$

where $\bar{z} = \xi_z / \dot{\xi}_z$ is the effective distance between the gate and the 2DEG. Current $i_{xz} \propto \dot{\xi}_x \dot{\xi}_z$ is induced by both the horizontal and the perpendicular fields, while $i_{xx} \propto \xi_x \dot{\xi}_x$ is only from the horizontal field which is similar to that in a SBD.

The responsivity can be greatly enhanced by optimizing the channel electron mobility, channel geometry, and antenna efficiency. The current responsivity can be expressed as

$$R_i = \frac{i_{xz} + i_{xx}}{P_0} = \frac{e\mu W}{2L} Z_0 \left\{ \bar{z} \int_0^L \frac{dn}{dV_{\text{geff}}} \dot{\xi}_x \dot{\xi}_z \cos \phi \, dx - \int_0^L \frac{dn}{dV_{\text{geff}}} \xi_x \dot{\xi}_x \, dx \right\}. \quad (2.33)$$

Equations (2.31) and (2.32) can be numerically calculated as a function of the gate voltage and the source-drain bias. As will be shown in Chap. 3, i_{xz} is usually the dominant self-mixing signal. For the special case when $V_{ds} = 0$ V, according to Eq. (2.23), the effective gate voltage and the electron density are $V_{\text{geff}} = V_g - V_{th}$ and $n = G_0 L / e\mu W$, respectively. The total self-mixing current under zero source-drain bias can be written as

$$i_0 = \frac{Z_0 P_0}{2} \frac{dG_0}{dV_{\text{geff}}} \left\{ \bar{z} \int_0^L \dot{\xi}_x \dot{\xi}_z \cos \phi \, dx - \int_0^L \xi_x \dot{\xi}_x \, dx \right\}. \quad (2.34)$$

The integral is independent on the gate voltage and is determined by the terahertz electric field distribution. Antenna is commonly used to manipulate the terahertz electric field. Hence, we define the integral as antenna factor A_0 which characterizes the enhancement of the terahertz electric fields,

$$A_0 = \bar{z} \int_0^L \dot{\xi}_x \dot{\xi}_z \cos \phi \, dx - \int_0^L \xi_x \dot{\xi}_x \, dx. \quad (2.35)$$

The self-mixing photocurrent under zero bias can be simplified as

$$i_0 = A_0 \times \frac{Z_0 P_0}{2} \frac{dG_0}{dV_{\text{geff}}}. \quad (2.36)$$

According to the Ohm's law, the photovoltage under zero bias can be expressed as

$$v_0 = A_0 \times \frac{Z_0 P_0}{2G_0} \frac{dG_0}{dV_{\text{geff}}}. \quad (2.37)$$

Similarly, under zero source–drain bias, the responsivity is in a simple form

$$R_i = A_0 \times \frac{Z_0}{2} \frac{dG_0}{dV_{\text{geff}}}. \quad (2.38)$$

As shown in Fig. 2.6, the effects of the series resistance of the detector and the input impedance of the voltmeter (r_{mv}) or the current meter (r_{mc}) affect the measurement of the photocurrent or the photovoltage. The measured conductance including the series resistance is $G_m = G_0/(1 + 2r_1G_0)$. The current meter and the voltmeter measure only a fraction of the photocurrent i_0 and the photovoltage $v_0 = i_0/G_0$. The photocurrent and photovoltage under zero bias can be expressed as

$$i_m = A_0 \times \frac{Z_0 P_0}{2} \frac{1}{(2r_1 + r_{mc})(1 - 2r_1G_m)G_m + (1 - 2r_1G_m)^2} \frac{dG_m}{dV_{\text{geff}}}, \quad (2.39)$$

$$v_m = A_0 \times \frac{Z_0 P_0}{2} \frac{r_{mv}}{(2r_1 + r_{mv})(1 - 2r_1G_m)G_m + (1 - 2r_1G_m)^2} \frac{dG_m}{dV_{\text{geff}}}. \quad (2.40)$$

When the detector noise is dominated by the thermal noise, the noise-equivalent power (NEP) of the detector can be expressed as

$$NEP = \begin{cases} \frac{N_{iB}}{R_i} = \frac{\sqrt{4k_B T G_m}}{i_m/P_0}, & \text{for photocurrent readout,} \\ \frac{N_{vB}}{R_v} = \frac{\sqrt{4k_B T/G_m}}{v_m/P_0}, & \text{for photovoltage readout,} \end{cases}$$

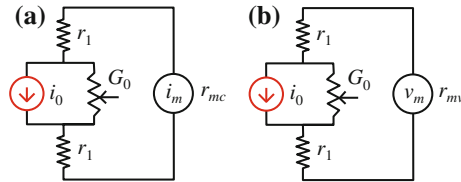


Fig. 2.6 Equivalent circuits for the detector when its **a** short-circuit photocurrent and **b** open-circuit photovoltage is considered, respectively. The series resistance of the detector (r_1) and the input impedance of the amplifiers (r_{mc} and r_{mv}) are included as well

where, T is the temperature, k_B is the Boltzmann constant, N_{iB} and N_{vB} are spectral noise current and noise voltage, respectively. The measured current responsivity and the measured voltage responsivity are defined as $R_i = i_m/P_0$ and $R_v = v_m/P_0$, respectively. It is clear that the series resistance decreases the responsivity and increases the noise-equivalent power.

2.3 Simulation of Terahertz Antenna by Using FDTD Method

Based on the above quasi-static self-mixing model, the responsivity is determined by two factors. One of the factors is directly related to the degree of controlling the electron density by the gate voltage dn/dV_{eff} , which is all about the field-effect and can be improved by enhancing the electron mobility, the gate capacitance and the geometry of the gate. The other factor is named as self-mixing factor $\dot{\xi}_x \dot{\xi}_z \cos \phi$, which is determined by the design of the antennas. Therefore, an optimized design of the antennas becomes crucial to increase the responsivity. In this section, the Finite-Difference in Time Domain (FDTD) method is introduced for antenna simulations.

2.3.1 Principle of FDTD and the Algorithm

In general, FDTD methods belong to the class of finite-element methods for numerically solving differential equations [24]. Proposed by Yee in 1966 [25], FDTD has been developed rapidly into a wide range of tools and applications such as FDTD Solutions, CST Microwave Studio, HFSS, EastFDTD, etc. FDTD solutions cover a wide frequency range with a single simulation run and treat nonlinear material properties in a natural way. FDTD method is widely used for numerical analysis of electrodynamics.

The time-dependent Maxwell's equations are discretized using central-difference approximations to the space and time partial derivatives. The resulting finite-difference equations are solved in either software or hardware in a leapfrog manner. The electric field vector components in a volume of space are solved at a given instant of time. Then the magnetic field vector components in the same spatial volume are solved at the next instant of time. These two processes are repeated over and over until the desired transient or steady-state electromagnetic field behavior is fully evolved.

It is worthwhile to introduce the method of finite difference. Setting the variable $\Delta x = h$ for function $f(x)$, the forward difference of $f(x)$ is

$$\Delta f = f(x + h) - f(x). \quad (2.41)$$

The derivative of $f(x)$ can be expressed in terms of the forward difference, the backward difference, and the center difference

$$\frac{df}{dx} = \lim_{\Delta x \rightarrow 0} \frac{\Delta f(x)}{\Delta x} \simeq \begin{cases} \frac{f(x+h)-f(x)}{h} & \text{forward} \\ \frac{f(x)-f(x-h)}{h} & \text{backward} \\ \frac{f(x+h)-f(x-h)}{2h} & \text{center} \end{cases} \quad (2.42)$$

According to the Taylor expansion, we get

$$f(x+h) = f(x) + h \frac{df(x)}{dx} + \frac{1}{2!} h^2 \frac{d^2 f(x)}{dx^2} + \frac{1}{3!} h^3 \frac{d^3 f(x)}{dx^3} + \dots \quad (2.43)$$

$$f(x-h) = f(x) - h \frac{df(x)}{dx} + \frac{1}{2!} h^2 \frac{d^2 f(x)}{dx^2} - \frac{1}{3!} h^3 \frac{d^3 f(x)}{dx^3} + \dots \quad (2.44)$$

$$f(x+h) - f(x-h) = 2h \frac{df(x)}{dx} + \frac{2}{3!} h^3 \frac{d^3 f(x)}{dx^3} + \dots \quad (2.45)$$

The central-difference approximation has an error which is proportional to the quadratic term of h .

The time-dependent Maxwell's equations are

$$\nabla \times \mathbf{H} = \frac{\partial \mathbf{D}}{\partial t} + \mathbf{J} \quad (2.46)$$

$$\nabla \times \mathbf{E} = -\frac{\partial \mathbf{B}}{\partial t} - \mathbf{J}_m \quad (2.47)$$

where \mathbf{E} is the electric field, \mathbf{D} is the displacement field, \mathbf{H} is the magnetic field strength, \mathbf{B} is the magnetic flux density, \mathbf{J} is the current density, \mathbf{J}_m is the magnetic flux density, ε is the dielectric constant, μ is the magnetic permeability, σ is the electrical conductivity, σ_m is the magnetic permeability.

In Cartesian coordinates, Eq. (2.47) can be written as

$$\begin{aligned} \frac{\partial H_z}{\partial y} - \frac{\partial H_y}{\partial z} &= \varepsilon \frac{\partial E_x}{\partial t} + \sigma E_x, \\ \frac{\partial H_x}{\partial z} - \frac{\partial H_z}{\partial x} &= \varepsilon \frac{\partial E_y}{\partial t} + \sigma E_y, \\ \frac{\partial H_y}{\partial x} - \frac{\partial H_x}{\partial y} &= \varepsilon \frac{\partial E_z}{\partial t} + \sigma E_z, \end{aligned} \quad (2.48)$$

and

$$\begin{aligned}\frac{\partial E_z}{\partial y} - \frac{\partial E_y}{\partial z} &= -\mu \frac{\partial H_x}{\partial t} - \sigma_m H_x, \\ \frac{\partial E_x}{\partial z} - \frac{\partial E_z}{\partial x} &= -\mu \frac{\partial H_y}{\partial t} - \sigma_m H_y, \\ \frac{\partial E_y}{\partial x} - \frac{\partial E_x}{\partial y} &= -\mu \frac{\partial H_z}{\partial t} - \sigma_m H_z.\end{aligned}\quad (2.49)$$

Equations (2.48) and (2.49) can be rewritten in a form of the central-difference. Define $f(x, y, z, t)$ as one component of \mathbf{E} and \mathbf{H} in Cartesian coordinates, and discretize it in time domain and the space domain with grid number n as

$$f(x, y, z, t) = f(i\Delta x, j\Delta y, k\Delta z, n\Delta t) = f^n(i, j, k). \quad (2.50)$$

The partial derivative can be approximated by the central differences,

$$\left. \frac{\partial f(x, y, z, t)}{\partial x} \right|_{x=i\Delta x} \simeq \frac{f^n(i + \frac{1}{2}, j, k) - f^n(i - \frac{1}{2}, j, k)}{\Delta x} \quad (2.51)$$

$$\left. \frac{\partial f(x, y, z, t)}{\partial y} \right|_{y=i\Delta y} \simeq \frac{f^n(i, j + \frac{1}{2}, k) - f^n(i, j - \frac{1}{2}, k)}{\Delta y} \quad (2.52)$$

$$\left. \frac{\partial f(x, y, z, t)}{\partial z} \right|_{z=i\Delta z} \simeq \frac{f^n(i, j, k + \frac{1}{2}) - f^n(i, j, k - \frac{1}{2})}{\Delta z} \quad (2.53)$$

Yee cellular in FDTD algorithm is shown in Fig. 2.7. Each magnetic field vector component is surrounded by four electric field vector components in a loop. Similarly, each electric field vector component is surrounded by four magnetic field vector components. This spatial sampling method of the electromagnetic components not only conforms to Faraday's law and Ampere's law, but is also suitable for difference calculation of the Maxwell equations and properly describes the propagation of

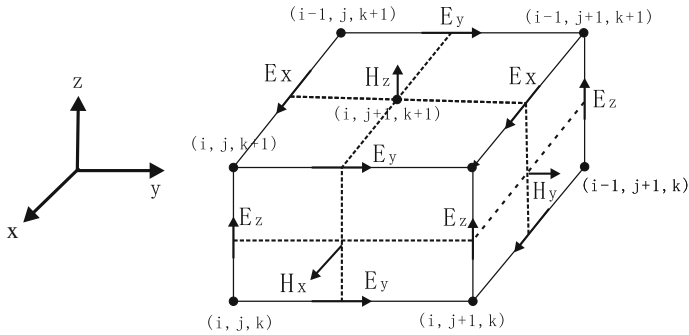


Fig. 2.7 Yee cellular in FDTD algorithm

electromagnetic wave. In addition, the sampling of the electric field and the magnetic field alternate in time domain, the sampling time intervals differ from each other by a half-time step. In this way, the Maxwell's equations become explicit difference equations and can be iteratively solved in the time domain. The space distribution of the electromagnetic field at each time step can be gradually calculated with given initial values and boundary conditions.

2.3.2 Antenna Simulation by FDTD

Dipole antennas have been widely used in microwave and radio frequency fields. Here, dipole antennas will be used to manipulate the near-field terahertz wave in the gated electron channel [16, 17]. FDTD simulations will be performed to evaluate the spatial distribution of the terahertz electromagnetic wave and its phase in the near-field zones of a symmetric and an asymmetric antenna.

A typical symmetric antenna on top of a GaN substrate is shown in Fig. 2.8. It contains a pair of metal dipole blocks each of which has a length of $45\ \mu\text{m}$ and a width of $10\ \mu\text{m}$. The length is about a quarter of the wavelength of the terahertz electromagnetic wave at 900 GHz. The width of the electron channel (2DEG mesa) under the antenna is $4\ \mu\text{m}$. The field-effect gate with a length of $2\ \mu\text{m}$ is inserted in between the two dipole blocks and the spacing between the gate and the antennas is $1.5\ \mu\text{m}$.

The spatial distributions of the terahertz electric field and the phase distributions at 900 GHz about 23 nm below the antennas are simulated using the FDTD method. The field enhancement factors for the horizontal and the perpendicular field are shown in Fig. 2.9a, b, respectively. The horizontal field is concentrated in the gaps between the gate and the antennas, while the perpendicular field is mainly distributed under the gate. The spatial distributions of the field strength are symmetric. However, the perpendicular field vanishes and changes its phase by π at $x \approx 0\ \mu\text{m}$, while the horizontal field keeps its phase constant along the channel, as shown in Fig. 2.9c, d. In Fig. 2.9e, the simulated mixing factor is plotted to reveal the spatial distribution of self-mixing. Strong self-mixing with a factor of 2,000 occurs mainly in the edge areas of the gated electron channel. The length of the active area where self-mixing

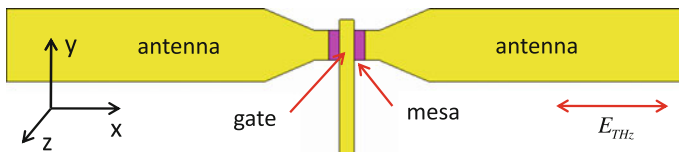


Fig. 2.8 A typical symmetric antenna with two dipole blocks and a gate. The 2DEG channel is under the gate and is connected to the dipole blocks

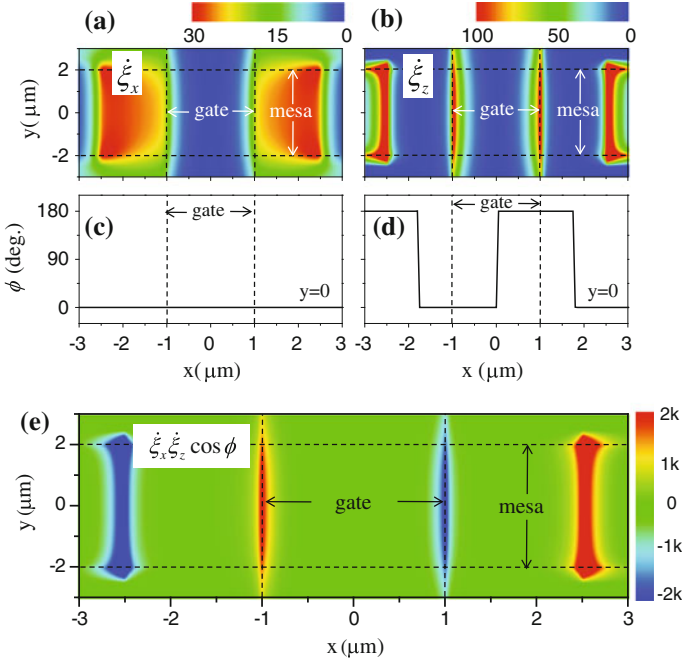


Fig. 2.9 Spatial distributions of the terahertz electric field and the phase simulated using FDTD method at 900 GHz. **a** Field enhancement factor $\dot{\xi}_x$ along the channel. **b** Field enhancement factor $\dot{\xi}_z$ perpendicular to the channel. **c, d** Phase ϕ_x and ϕ_z at $y = 0$. **e** Mixing factor $\dot{\xi}_x \dot{\xi}_z \cos \phi$

is predominant is about 200 nm and is only one-tenth of the gate length. Due to the phase change at $x = 0 \mu\text{m}$, the mixing at the source side generates a photocurrent opposite to that induced at the drain side. With a symmetric design of the antennas, the overall photocurrent vanishes. Hence, a symmetric antenna design is not favorable for high sensitivity detection.

An asymmetric antenna design consisting of three dipole blocks is shown in Fig. 2.10. Similar to those shown in Fig. 2.8, each dipole block (A, B and C) is $45 \mu\text{m} \times 10 \mu\text{m}$, the gate length is $2 \mu\text{m}$, and the gap between the gate and the two isolated blocks (A and B) is $1.5 \mu\text{m}$. Block C is used to induce asymmetric terahertz electric field in the gated electron channel.

As shown in Fig. 2.11a, b, the horizontal field is concentrated in the gaps between the gate and block A/B, while the perpendicular field is mainly distributed under the gate. Both fields are stronger at the left side of the gate than at the right side. The horizontal field vanishes and changes its phase by π at $x \approx +0.3 \mu\text{m}$, while the perpendicular field keeps its phase constant along the channel as shown in Fig. 2.11c, d. Similar to that shown in Fig. 2.9e, self-mixing is highly localized near the edges of the gated electron channel, as shown in Fig. 2.11e. The mixing factor $\dot{\xi}_x \dot{\xi}_z \cos \phi$ at the left side and the right side are about 10,000 and 2,000, respectively. Self-mixing is greatly enhanced by the asymmetric design. Most importantly, the asymmetric

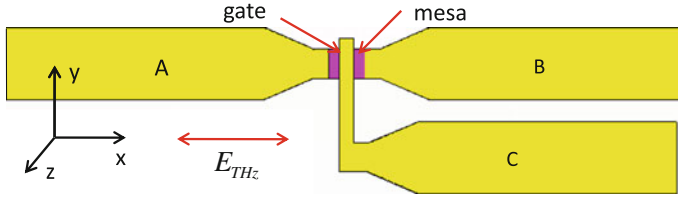


Fig. 2.10 Asymmetric antenna consists of three dipole blocks A, B, and C

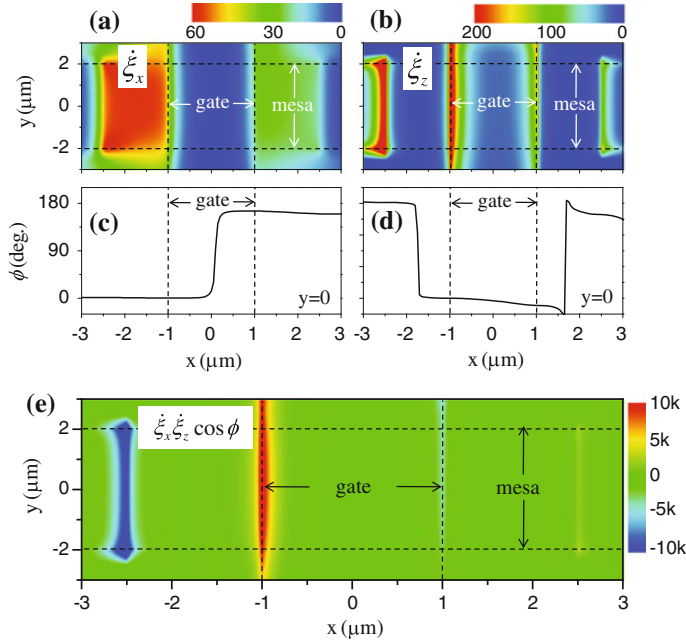


Fig. 2.11 Terahertz field distribution in the near-field zone of an asymmetric antenna designed for 900 GHz. Spatial distributions of the field enhancement factors (a, b) and the phases (c, d) of the horizontal and the perpendicular field. e Spatial distribution of the mixing factor $\xi_x \xi_z \cos \phi$

design allows for the generation of photocurrent predominantly determined by the self-mixing in one of the two active regions. Asymmetric antenna design is crucial for high responsivity terahertz detection.

The aspect ratio of the antenna width (AW) and the antenna length (AL) affects the self-mixing factor at the resonant frequency. The resonant frequency and the mixing factor as a function of the block length (AL) while the antenna width is fixed at $10 \mu\text{m}$ is shown in Fig. 2.12a. With increasing the antenna length from $10 \mu\text{m}$ to $120 \mu\text{m}$, the mixing factor $\xi_x \xi_z \cos \phi$ is enhanced from 500 to 90,000 and the resonant frequency decreases from 1,740 to 380 GHz. The resonant frequency and the mixing factor as a function of the antenna width while the length width is fixed at $45 \mu\text{m}$ is shown in Fig. 2.12b. By increasing the antenna width from 4 to $20 \mu\text{m}$, the mixing

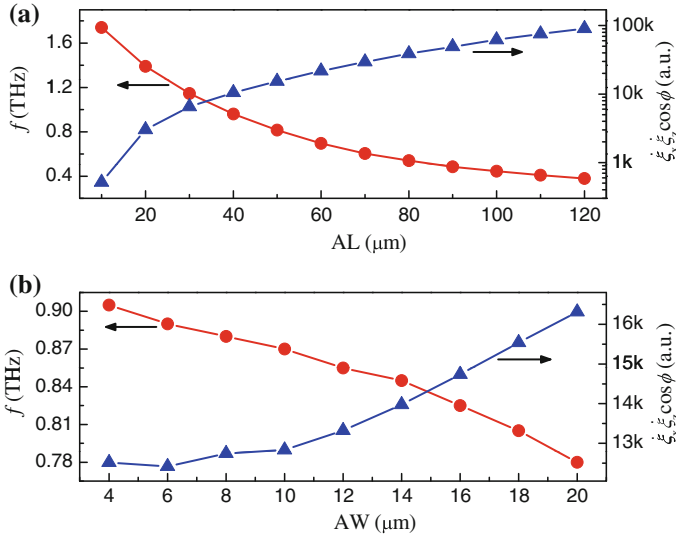


Fig. 2.12 Resonant frequency and mixing factor as a function of **a** the length (AL) and **b** the width (AW) of the antenna blocks. The width and the length are set as 10 and 45 μm for (a) and (b), respectively

factor $\xi_x \xi_z \cos \phi$ increases slightly from 12,500 to 16,300 and the resonant frequency decreases from 905 to 780 GHz. The antenna length is the main factor affecting the self-mixing factor. Furthermore, the mixing factor of this 3-block antenna designed for lower resonant frequencies is much larger than that at higher resonant frequencies.

2.3.3 Terahertz Filter

The resonant characteristics of the antenna are vulnerable to any nearby metallic structures, such as bonding pads and the interconnection between the pads and the antenna blocks. The effect of the bonding pads on the self-mixing factor is simulated and is shown in Fig. 2.13. The horizontal and the perpendicular electric field are about 400 and 20 at the resonant frequency 1 THz, respectively. In the case when the antennas and the bonding pads are connected via straight metal lines as shown in Fig. 2.13b, the maximum perpendicular field decreases from 400 to 180 and an extra resonance around 200 GHz is induced. To eliminate this negative effect of bonding pads on the mixing factor and hence the responsivity, we use low pass filters as interconnection between the antenna blocks and the bonding pads, as shown in Fig. 2.13c. Simulations indicate that by isolating the antennas from the bonding pads the self-mixing factor can be restored to its original value as that shown in Fig. 2.13a.

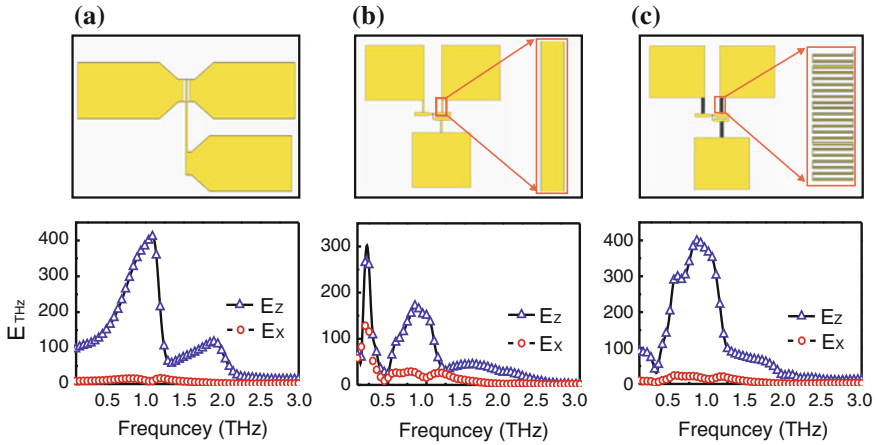


Fig. 2.13 Terahertz electric fields as a function of the frequency. **a** Asymmetric antenna without any bonding pad. **b** Asymmetric antenna with bonding pads connected to each antenna block by a straight metal line. **c** Asymmetric antenna with terahertz filters connecting the antenna blocks and the bonding pads. The filter is meander shaped. Reprinted with permission of Ref. [18], copyright 2011, American Institute of Physics

Therefore, the meander-shaped low pass filters connecting the antenna with the corresponding bonding pad can maintain the mixing factor and ensure a good performance for *NEP*. Simulations also suggest that the isolation effect can be enhanced by increasing the length of the filter. For the meander-shaped filter, the filter effect can be optimized when the periodicity is more than 25. A scanning electron microscope graph shown in Fig. 2.14 is such a terahertz filter with a line width of 150 nm, a width of 500 nm and a periodicity of 30.

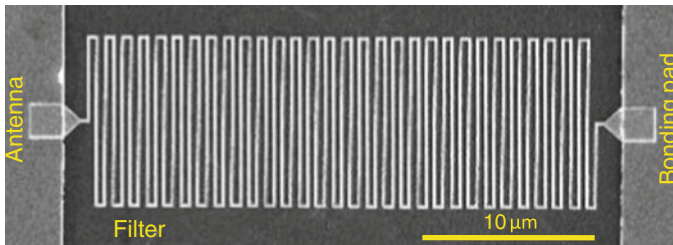


Fig. 2.14 Scanning electron microscope photograph of a meander shaped low pass filter

2.4 Summary

We summarize the existing theories on terahertz detection in field-effect electron channel based on the time-dependent hydrodynamic transport equation and the continuity equation with asymmetric boundary conditions either for the zero-biased or the biased situations. We develop a quasi-static self-mixing detector model based on the gradual channel approximation. The model takes into account the spatial distributions of terahertz electric fields and the electron density in the gated electron channel. Numerical calculations can be made based on this model to present quantitative terahertz photoresponse in the linear regime, the saturation regime, the transition regime, and the pinch-off regime. According to the model, the terahertz photoresponse is proportional to the local derivative of the electron density dn_x/dV_g and the mixing factor $\xi_x \xi_z \cos \phi$. Symmetric and asymmetric antennas made of multiple dipole blocks are designed to manipulate the local terahertz field distribution and near-field enhancement. Simulations of the terahertz antennas reveal that the self-mixing factor is greatly enhanced in the left and right edge areas of the gated electron channel. The phase flip of π of the perpendicular terahertz field across the gated electron channel induces a photocurrent in the left edge area opposite in direction to that induced within the right edge area. An asymmetric antenna design allows for optimization of the overall photocurrent according to the structural factor $\int_0^L \xi_x \xi_z \cos \phi \, dx$.

For realistic design of an antenna coupled self-mixing detector, the influence of bonding pads on the antenna response and the near-field enhancement are evaluated. Meander-shaped low-pass filters are applied to effectively isolate the antenna blocks from the metallic bonding pads. In the next chapter, the physical realization of self-mixing terahertz detectors based on AlGaIn/GaN field-effect transistors with terahertz antennas will be introduced in detail.

References

1. Dyakonov, M., Shur, M.S.: Shallow water analogy for a ballistic field effect transistor: new mechanism of plasma wave generation by dc current. *Phys. Rev. Lett.* **71**, 2465 (1993)
2. Dyakonov, M., Shur, M.S.: Detection, mixing, and frequency multiplication of terahertz radiation by two-dimensional electronic fluid. *IEEE Trans. Electron Devices* **43**(3), 380–387 (1996)
3. Lü, J.Q., Shur, M.S., Hesler, J.L., Liangquan, S., Weikle, R.: Terahertz detector utilizing two-dimensional electronic fluid. *IEEE Electron Device Lett.* **19**(10), 373–375 (1998)
4. Lü, J.Q., Shur, M.S.: Terahertz detection by high-electron-mobility transistor: enhancement by drain bias. *Appl. Phys. Lett.* **78**, 2587 (2001)
5. Tauk, R., Teppe, F., Boubanga, S., Coquillat, D., Knap, W., Meziani, Y.M., Gallon, C., Boeuf, F., Skotnicki, T., Fenouillet-Beranger, C., Maude, D.K., Rumyantseva, S., Shur, M.S.: Plasma wave detection of terahertz radiation by silicon field effects transistors: responsivity and noise equivalent power. *Appl. Phys. Lett.* **89**(25), 253511 (2006)
6. Knap, W., Dyakonov, M., Coquillat, D., Teppe, F., Dyakonova, N., Sakowski, J., Karpierz, K., Sakowicz, M., Valusis, G., Seliuta, D., Kasalynas, I., El Fatimy, A.: Field effect transistor for

- terahertz detection: physics and first imaging applications. *J. Infrared Millim. Terahz Waves* **30**(12), 1319–1337 (2009)
7. Knap, W., Teppe, F., Meziani, Y., Dyakonova, N., Lusakowski, J., Buf, F., Skotnicki, T., Maude, D., Rumyantsev, S., Shur, M.S.: Plasma wave detection of sub-terahertz and terahertz radiation by silicon field-effect transistors. *Appl. Phys. Lett.* **85**, 675 (2004)
 8. Lissauskas, A., Pfeiffer, U., Öjefors, E., Bolivar, P.H., Glaab, D., Roskos, H.G.: Rational design of high-responsivity detectors of terahertz radiation based on distributed self-mixing in silicon field-effect transistors. *J. Appl. Phys.* **105**, 114511 (2009)
 9. Knap, W., Rumyantsev, S., Lu, J., Shur, M., Saylor, C., Brunel, L.: Resonant detection of subterahertz radiation by plasma waves in a submicron field-effect transistor. *Appl. Phys. Lett.* **80**, 3433 (2002)
 10. El Fatimy, A., Teppe, F., Dyakonova, N., Knap, W., Seliuta, D., Valuis, G., Shchepetov, A., Roelens, Y., Bollaert, S., Cappy, A., Rumyantsev, S.: Resonant and voltage-tunable terahertz detection in InGaAs/InP nanometer transistors. *Appl. Phys. Lett.* **89**, 131926 (2006)
 11. Popov, V.V., Polischuk, O.V., Knap, W., El Fatimy, A.: Broadening of the plasmon resonance due to plasmon-plasmon intermode scattering in terahertz high-electron-mobility transistors. *Appl. Phys. Lett.* **93**, 263503 (2008)
 12. Peralta, X.G., Allen, S.J., Wanke, M.C., Harff, N.E., Simmons, J.A., Lilly, M.P., Reno, J.L., Burke, P.J., Eisenstein, J.P.: Terahertz photoconductivity and plasmon modes in double-quantum-well field-effect transistors. *Appl. Phys. Lett.* **81**, 1627 (2002)
 13. Dyer, G.C., Vinh, N.Q., Allen, S.J., Aizin, G.R., Mikalopas, J., Reno, J.L., Shaner, E.A.: A terahertz plasmon cavity detector. *Appl. Phys. Lett.* **97**, 193507 (2010)
 14. Dyer, G.C., Aizin, G.R., Allen, S.J., Grine, A.D., Bethke, D., Reno, J.L., Shaner, E.A.: Induced transparency by coupling of Tamm and defect states in tunable terahertz plasmonic crystals. *Nat. Photonics* **7**, 925–930 (2013)
 15. Veksler, D., Teppe, F., Dmitriev, A.P., Kachorovskii, V.Yu., Knap, W., Shur, M.S.: Detection of terahertz radiation in gated two-dimensional structures governed by dc current. *Phys. Rev. B* **73**, 125328 (2006)
 16. Sun, J.D., Qin, H., Lewis, R.A., Sun, Y.F., Zhang, X.Y., Cai, Y., Wu, D.M., Zhang, B.S.: Probing and modelling the localized self-mixing in a GaN/AlGaIn field-effect terahertz detector. *Appl. Phys. Lett.* **100**, 173513 (2012)
 17. Sun, J.D., Sun, Y.F., Wu, D.M., Cai, Y., Qin, H., Zhang, B.S.: High-responsivity, low-noise, room-temperature, self-mixing terahertz detector realized using floating antennas on a GaN-based field-effect transistor. *Appl. Phys. Lett.* **100**, 013506 (2012)
 18. Sun, Y.F., Sun, J.D., Zhou, Y., Tan, R.B., Zeng, C.H., Xue, W., Qin, H., Zhang, B.S., Wu, D.M.: Room temperature GaN/AlGaIn self-mixing terahertz detector enhanced by resonant antennas. *Appl. Phys. Lett.* **98**, 252103 (2011)
 19. Sun, J.D., Sun, Y.F., Zhou, Y., Zhang, Z.P., Lin, W.K., C.H., Zeng, W., D.M., Zhang, B.S., Qin, H., Li, L.L., Xu, W.: Enhancement of terahertz coupling efficiency by improved antenna design in GaN/AlGaIn HEMT detectors. *AIP Conf. Proc.* **1399**, 893 (2011)
 20. Zhou, Y., Sun, J.D., Sun, Y.F., Zhang, Z.P., Lin, W.K., Lou, H.X., Zeng, C.H., Lu, M., Cai, Y., Wu, D.M., Lou, S.T., Qin, H., Zhang, B.S.: Characterization of a room temperature terahertz detector based on a GaN/AlGaIn HEMT. *J. Semicond.* **32**(4), 064005 (2011)
 21. Sun, J.D., Qin, H., Lewis, R.A., Yang, X.X., Sun, Y.F., Zhang, Z.P., Li, X.X., Zhang, X.Y., Cai, Y., Wu, D.M., Zhang, B.S.: The effect of symmetry on resonant and nonresonant photore-sponses in a field-effect terahertz detector. *Appl. Phys. Lett.* **106**, 031119 (2015)
 22. Lü, L., Sun, J.D., Lewis, R.A., Sun, Y.F., Wu, D.M., Cai, Y., Qin, H.: Mapping an on-chip terahertz antenna by a scanning near-field probe and a fixed field-effect transistor. *Chin. Phys. B* **24**(2), 028504 (2015)
 23. Brews, J.R.: A charge-sheet model of the MOSFET. *Solid State Electron.* **21**(2), 345–355 (1978)
 24. Taflov, A., Hagness, S.C.: *Computational Electrodynamics: the Finite-difference Time-domain Method*, 3rd edn. Artech House, Boston (2005)
 25. Yee, K.: Numerical solution of initial boundary value problems involving Maxwell's equations in isotropic media. *IEEE Trans. Antennas Propag.* **14**(2), 302–307 (1966)

Field-effect Self-mixing Terahertz Detectors

Sun, J.

2016, XVIII, 126 p. 84 illus., 4 illus. in color., Hardcover

ISBN: 978-3-662-48679-5